Antiferromagnetic spin and twin domain walls govern hysteretic expressions of exchange anisotropy

Jason N. Armstrong, Matthew R. Sullivan, and Harsh Deep Chopra*
Laboratory for Quantum Devices, Materials Program, Mechanical & Aerospace Engineering Department, State University of New York at Buffalo, Buffalo, New York 14260, USA
(Received 13 May 2009; revised manuscript received 29 July 2009; published 24 September 2009)

The present study shows that antiferromagnetic spin and twin domain walls govern the hysteretic expressions of exchange anisotropy at low and high fields, respectively, using annealed NiO single crystals and Co. In the presence of twin walls, spin walls are shown to be a geometrical necessity in the antiferromagnetic NiO. A threshold field (~10 000 Oe) exists below which twin walls are frozen, and rotational hysteresis is dominated by losses due to spin walls. Above the threshold field, twin walls become mobile, resulting in a sharp increase in rotational hysteresis. Remarkably, rotational hysteresis associated with spin walls is similar to that of an ordinary ferromagnet—as the field strength increases, rotational hysteresis tends toward zero. However, unlike an ordinary ferromagnet where rotational hysteresis becomes zero above its saturation field, rotational hysteresis in antiferromagnet drops but then sharply increases once the threshold field for twin wall motion is exceeded. In crystals without spin walls, low-field rotational hysteresis is zero or negligible. Domain imaging of twin walls in antiferromagnet and Weiss walls in ferromagnet reveals a one-to-one spatial correlation even though twin walls are considered to have no net dipoles. This surprising result is explained by the fact that crystallographic interfaces in real crystals are not atomically sharp or ideal, and the defective interface invariably results in net moment across the finite width of the twin wall. The field dependence of domain walls in Co film exchange coupled to NiO shows global similarities to previously reported behavior of Co films deposited on nanocrystalline NiO [H. D. Chopra, D. X. Yang, P. J. Chen, H. J. Brown, L. J. Swartzendruber, and W. F. Egelhoff, Jr., Phys. Rev. B **61**, 15312 (2000)]. In both cases, domain wall motion is not the dominant mode of magnetization reversal (wall motion is entirely absent in the present study while wall motion was only occasionally observed in the previous study), reversal occurs abruptly and different regions switch at different fields, and the observed pinning sites are frozen in the applied field range. Despite vastly different underlying microstructure of NiO in these two studies (annealed NiO single crystal with a fixed orientation across the NiO-Co interface in the present study versus nanocrystalline NiO in the previous study), the observed similarities may be understood by recognizing that, just as crystallographically imperfect twin interfaces serve as pinning sites for walls in Co film, other defects can play a similar role. Practically, results provide means of tuning rotational hysteresis by varying the type and the density of domain walls in NiO and by tuning the saturation field of the ferromagnet relative to the threshold field for the twin wall motion.

DOI: 10.1103/PhysRevB.80.104429 PACS number(s): 75.60.Ch, 75.60.Ej, 75.70.Kw

I. INTRODUCTION

In fundamental investigations of physical phenomena, the use of single crystals eliminates complications arising from interfaces. Single crystals are also often used for controlled incorporation of interface(s) to study the structure sensitivity of a given property, such as, for example, the use of bicrystals or tricrystals to investigate phenomena related to magnetism, electron transport, superconductivity, deformation, etc.; see, for example, Refs. 1–5. In particular, several studies[6–15] have previously utilized antiferromagnetic single crystals to investigate the origins and various expressions of exchange anisotropy arising from coupling between an antiferromagnet and a ferromagnet.[16–18] The scientific and technological significance of exchange anisotropy was immediately apparent to Meiklejohn and Bean when they first reported this effect.[16–18] Since its discovery, various expressions of exchange anisotropy have been found, including *unidirectional* anisotropy,[16–19] sin θ torque curves,[17] rotational hysteresis in fields greater than saturation fields for ferromagnets,[17] enhanced coercivty,[20] decay in width of hysteresis loops with repeated cycling,[21–24] etc. In addition, exchange anisotropy has also been observed in ferrimagnetic-ferromagnetic[25] and ferrimagnetic-antiferromagnetic[26] exchange coupled systems. These investigations have led to new fundamental insights into the physics of magnetism and means of creating new forms of synthetic magnets. The interactions between spins in materials with different magnetic orders may also be used to engineer practical magnetic properties of materials. Indeed, exchange anisotropy has proven to be a key element in the devices utilizing spin-dependent electron transport, such as giant magnetoresistance spin valves.[27,28]

Consider an *ideal single crystal* of NiO, which is the antiferromagnetic material used in the present study. As shown schematically in Fig. 1, the spin structure of NiO consists of ferromagnetic Ni sheets on {111}-type planes,[29] with spins in adjacent Ni planes being antiparallel due to superexchange interactions across oxygen atoms.[30,31] The spin axis within each Ni sheet lies along the ⟨110⟩-type direction.[32] For example, with reference to the specific (111) planes shown in Fig. 1, the spin direction lies parallel and antiparallel to the $[\bar{1}10]$ direction in alternate planes. This spin structure is well established and confirmed by pioneering neutron-diffraction studies of Shull *et al.*[29] and Roth.[6,32,33] Figure 1 shows that

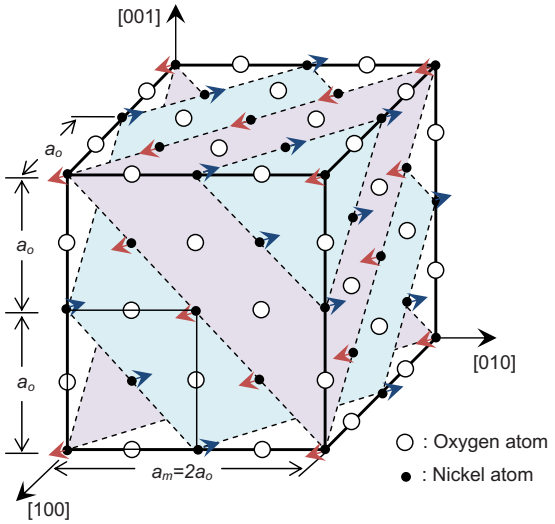

FIG. 1. (Color online) Schematic of the antiferromagnetic spin structure in NiO. The antiferromagnetic ordering below the Néel temperature (523 K) results in a slight rhombohedral distortion due to contraction along one of the four ⟨111⟩ axes in the cubic phase. Relative to a rhombohedral angle of 60° for the primitive unit cell of the paramagnetic cubic phase, the rhombohedral angle in the antiferromagnetic state is 60° 4.2′, and this small distortion is ignored in the schematic. Note that the magnetic unit cell is twice as large as the crystal unit cell.

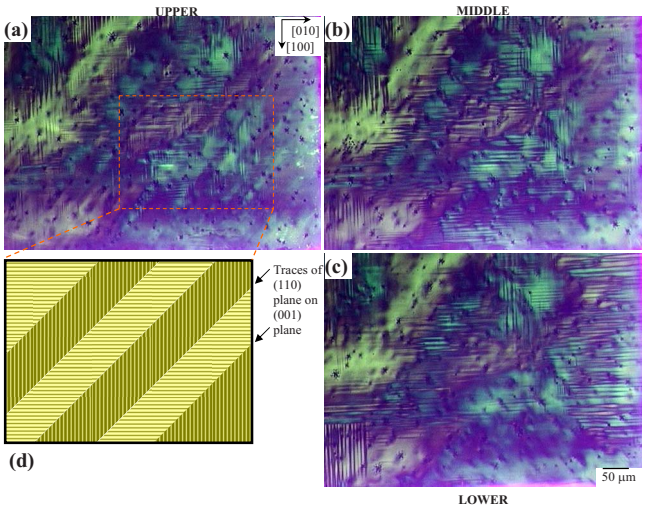

FIG. 2. (Color online) Platelets of twin domains on (100) and (010) planes of an as-grown NiO single crystal, viewed along the [001] crystal axis. The micrographs were recorded using transmitted polarized light. Micrographs (a)–(c) correspond to twin pattern near the top, middle, and bottom of the crystal, respectively. (d) Schematic of twin pattern in (a).

the *magnetic unit cell* is twice as large as the *crystal unit cell* ($a_m=2a_o$). In an ideal single crystal, the crystalline and magnetic periodicity would be repeated to infinity in three dimensions. Deviations from the ideal periodicity occur in the presence of long-range defects such as stacking faults, low-angle grain boundaries, twin boundaries, dislocations, etc., which breaks the translation symmetry of the crystal. Since the magnetic periodicity is linked to the crystalline periodicity, the presence of long-range crystalline defects also creates corresponding defects in the spin structure. For example, crystallographic twins give rise to antiferromagnetic twin domains. The same interface that separates adjacent crystallographic twins also serves as the wall (T wall) for the antiferromagnetic domains across which the spin motif changes orientation continuously along a common spin axis.[6] In fact, as-grown NiO single crystals are rarely homogeneous and have a cornucopia of twins.[34–36] This is shown in the transmitted polarized light optical micrographs of an as-grown NiO single crystal in Figs. 2(a)–2(c); details of imaging the twin domains by transmission polarized optical microscopy are given later in the Experimental Details section. Viewed along the [001] axis, Fig. 2(a) shows fine twin platelets (~1–5 μm thick) lying along the (100) and the (010) planes. A closer examination of the area enclosed in Fig. 2(a) shows that the twins are actually confined within bands that run diagonally at 45° across the (001) plane (plane of the figure). As shown schematically in Fig. 2(d), these bands are traces of the (110) planes intersecting the (001) crystal surface. It was found that Fig. 2(a) only represents twin plates near the upper half of the crystal. By focusing the microscope at different depths of the crystal, the varying profile of the twins was mapped, as shown in Figs. 2(a)–2(c) for the upper, the middle, and the lower sections of the crystal, respectively. Also note the large variation in color contrast in the micrographs, which is indicative of a high internal strain in the crystal to accommodate differently oriented twin variants.

The twins in NiO are formed as a result of self-strain associated with cubic to rhombohedral structural transformation that accompanies paramagnetic to antiferromagnetic phase transition at its Néel temperature (T_N=523 K).[37–40] Below the Néel temperature, antiferromagnetic ordering is accompanied by a slight rhombohedral contraction of any one of the four equivalent ⟨111⟩ directions of the parent cubic phase, with the antiferromagnetic sheets being normal to the contraction axis.[7] For example, the contraction axis in the schematic shown in Fig. 1 lies along the [111] direction corresponding to magnetic ordering on the (111) planes. With reference to the parent (cubic) phase, since all four ⟨111⟩ directions are crystallographically equivalent, contraction can randomly occur along different ⟨111⟩ directions in different volumes of the crystal, resulting in a heavily twinned structure of the type shown in Fig. 2. For ease of discussion in the following, supplementary document 1 lists all possible twin configurations corresponding to contraction along the four different ⟨111⟩ axes.[41] Note that the principle behind formation and motion of differently oriented variants of the low symmetry (rhombohedral) phase is analogous to structural twins formed in multiferroic materials, such as shape memory alloys, ferroelectrics, etc.

In general, the absence of grain boundaries suffices to describe a single crystal. It is implicitly assumed that barring the invariable presence of dislocations, point defects, or a low density of stacking faults and twins, the translation symmetry of the single crystal is essentially preserved across the entire volume of the crystal. From the micrographs shown in Fig. 2, it is clear that although this single-crystal sample is

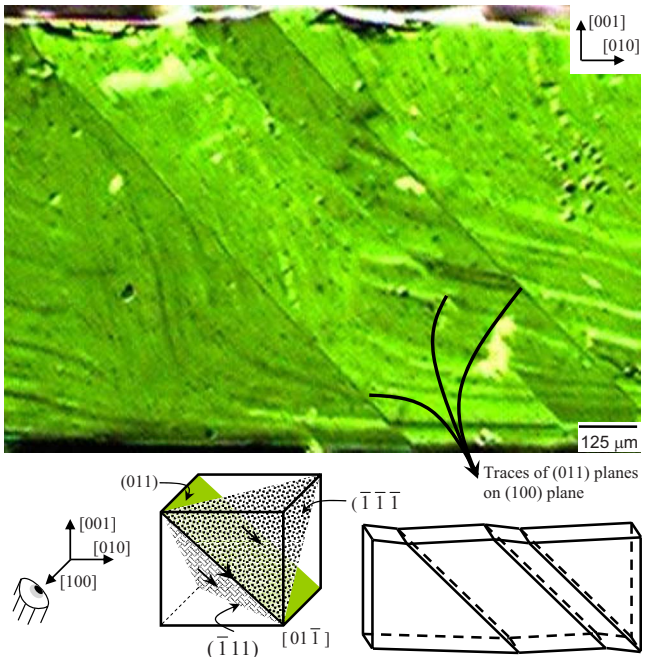

FIG. 3. (Color online) Plane parallel assembly of two twin variants, I($\bar{1}\bar{1}\bar{1}$)-IV($\bar{1}11$), in an annealed NiO single crystal viewed along the [100] crystal direction. The schematic in the lower left shows ferromagnetic Ni sheets on the ($\bar{1}11$) and ($\bar{1}\bar{1}\bar{1}$) planes, separated by (011) T wall. For clarity, Ni sheets with antiparallel spins are not shown. The schematic in lower right shows exaggerated relief on the crystal surface due to varying orientation of the rhombohedral contraction axes in adjacent twin domains.

free of grain boundaries, the high density of twins renders the crystal into a "paracrystalline" form (to distinguish it from random change in translation symmetry due to grain boundaries), in which the crystal symmetry is broken albeit accordingly to well-defined crystallographic rules of twinning. In such a crystal, the measured physical properties are an aggregate over different directions similar to a *textured* polycrystal and such a crystal is not amenable to single-crystal studies.

In the present study, heating the NiO crystal to its paramagnetic state followed by slow cooling did not reduce the high twin density. This is indicative of defects in the as-grown single crystals. Annealing can produce NiO single crystals with a low twin density.[6] Only after the crystals were annealed at high temperatures, the number of twins reduced drastically. Details of annealing, deposition conditions for Co film on NiO, optical imaging of antiferromagnetic twin domains in NiO and ferromagnetic domains in Co, as well as details of other magnetic characterization methods used in the present study are described in the following section followed by the discussion of the results.

II. EXPERIMENTAL DETAILS

An as-grown single crystal ($5\times5\times1$ mm^3) was cleaved with a knife edge along the {100} plane (the cleavage plane of NiO), with the typical thickness of cleaved crystals pieces being on the order of 100 μm and a few mm in lateral dimensions. The cleaved crystals were placed in an air furnace and heated to 1673–1773 K for 1–3 h followed by slow cooling (5 K/min) to room temperature. This heat treatment resulted in NiO single crystals with only a few large twins across the entire volume of the crystal. Care had to be taken in handling the resulting crystals to avoid accidental nucleation of twins due to forces generated by the tweezers. Instead, samples were transported using the adhesion force of a slightly moist tissue paper. It was found that, if the crystals were cooled to room temperature at a rapid or uncontrolled rate, say, by suddenly opening the furnace door, the resulting crystals had a relatively higher twin density and they were of high elastic energy variety due to uncontrollable simultaneous growth and subsequent impingement of twins in different volumes of the crystal. The behavior of such crystals in applied field is also discussed in the following section.

Annealed crystals were green in color, which is indicative of near stoichiometric composition (as opposed to pale yellow crystals that are oxygen rich).[42,43] The NiO crystals are optically anisotropic (birefringent) with optic axis parallel to the rhombohedral contraction experienced by the crystal upon antiferromagnetic ordering below the Néel temperature.[6] Therefore, in a twinned NiO crystal, the orientation of the optic axes changes upon crisscrossing from one T domain to another. Owing to this spatial variation of the optic axis, a sufficient contrast between adjacent T domains can be achieved by imaging the crystals using transmitted polarized light combined with a compensator or a wave plate (half-λ) to enhance the shift in the interference colors resulting from birefringence. The contrast between adjacent twin domains would vary depending on the relative orientation of their optic axes relative to the compensator plate. Obviously, in the trivial case of a twin-free NiO single crystal, the entire volume of the crystal has a single optic axis, and a uniform contrast is expected and observed.

The magnetic domain structure in Co film deposited on NiO crystals was studied using the high-resolution interference contrast colloid (ICC) method in the reflection mode,[44] and details of this technique are described elsewhere.[45–47] Briefly, the ICC method employs a colloidal solution to decorate the microfield on a magnetic surface, similar to the versatile Bitter method.[48] However, the technique differs in the manner in which the colloid decorated microfield is detected. In the Bitter method, a problem in contrasts develops in the bright-field or the dark-field mode due to backscattering by particles and various surfaces between the objective lens and the specimen, which results in an overall loss of resolution. Instead, the ICC method uses a Nomarski interferometer to detect the surface microfield distribution. The magnetic microfield on the surface causes local variation in the density of colloid particles (average colloid particle size is 7 nm), thereby delineating the domain structure. This microfield is detected in the reflection mode by polarization interferometer optics, which detects any unevenness at the nanometer scale and reveals domain structure with a pronounced three-dimensional effect and at a high resolution that is limited only by that of the microscope (0.4–0.6 μm).

Whereas domain in bare NiO crystals were imaged in transmission mode of the optical microscope, spatial corre-

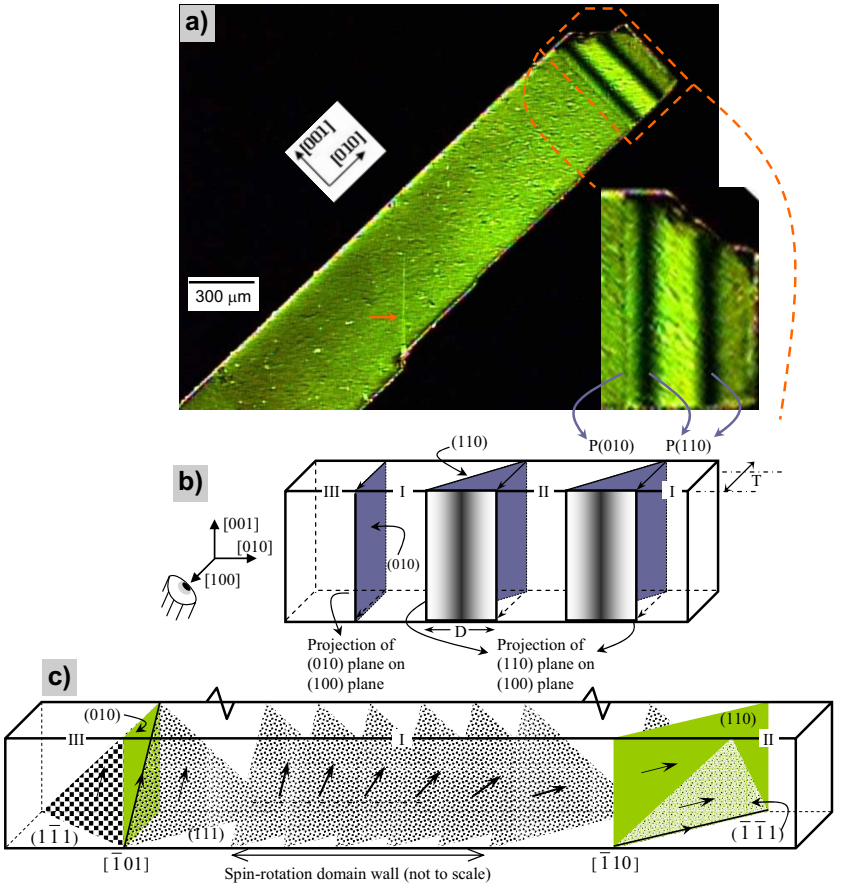

FIG. 4. (Color online) Presence of more than two twin variants necessitates the formation of S walls. (a) A nearly twin-free annealed NiO single crystal except for a few twins at the end. Inset shows magnified view of the twins at the end of the sample. [(b),(c)] The schematics show the crystallography and antiferromagnetic spin motif across twin domains, respectively. The position of the S wall is arbitrary and may coincide with the T walls. The width of the S wall is also exaggerated for clarity. For clarity, Ni sheets with antiparallel spins are not shown. See text for explanation.

lation between domains in Co film deposited over NiO was accomplished simply by switching the mode from transmission (for NiO) to reflection (for ICC imaging of Co). In such samples, the 10-nm-thick Co film was transparent enough for mapping the antiferromagnetic domains in NiO.

Cobalt films (10 nm thick) were deposited on NiO crystals and silicon substrates using dc magnetron sputtering. Sputtering was carried out in an Ar pressure of $\sim 8-10$ mTorr in a UHV system whose base pressure was in the $10^{-8}-10^{-9}$ Torr range. Samples were capped with $\sim$2.5-nm-thick Au or Ta protective layer to prevent oxidation over time. The torques curves as a function of applied field were measured at room temperature using Quantum Design physical property measurement system. For torque magnetometry, the twin structure of NiO crystals was recorded both prior and after the measurements in order to determine the effect of applied field on twin domain pattern.

III. RESULTS AND DISCUSSION

A. Spin walls as geometrically necessity in the presence of twin walls

The effect of annealing in drastically reducing the density of twin domains in NiO is shown in Fig. 3 (cf. Fig. 2). The sample in Fig. 3 consists of just four large twins. Viewed along the [100] axis, the lower left schematic in Fig. 3 shows that Ni sheets in adjacent twins lie on the $(\bar{1}11)$ and $(\bar{1}\bar{1}\bar{1})$ planes, separated by (011) T wall; for clarity Ni sheets with antiparallel spins are not shown. The key point of Fig. 3 is that this twin geometry consisting of two twin variants with a common magnetic axis, $[01\bar{1}]$, allows the spins in Ni sheets to change *continuously* from $(\bar{1}11)$ to $(\bar{1}\bar{1}\bar{1})$ plane. As a result, no spin-rotation walls (S walls) are needed in crisscrossing from one twin to another. With reference to supplementary document 1,[41] the twin configuration in Fig. 3 is referred to as I$(\bar{1}\bar{1}\bar{1})$-IV$(\bar{1}11)$; the supplementary document also shows all other possible twin variants with a common magnetic axis. The lower right schematic in Fig. 3 shows exaggerated relief on the crystal surface due to varying orientation of the rhombohedral contraction (optic) axis in the crystal, which enables adequate contrast between adjacent twins when viewed in transmitted polarized light.

Figures 4 and 5 are shown to highlight that, aside from a simple plane-parallel assembly of twins consisting of only two variants with a common magnetic axis (such as the one shown in Fig. 3 or in supplementary document 1),[41] three or more twin variants necessitate the formation of spin domain walls or S walls. The properties of S walls have previously been measured using neutron-diffraction and torque measurements.[6,7] While S walls cannot be seen optically, their presence can be easily deduced from Fig. 4. The annealed NiO single crystal in Fig. 4(a) is twin free over its entire length except for the few twins at the end and a tiny platelet in the middle (marked by the arrow). The inset in Fig. 4(a) is a magnified view of the twinned end of the crystal. The schematics in Figs. 4(b) and 4(c) show, respectively, the crystallography and the antiferromagnetic spin structure

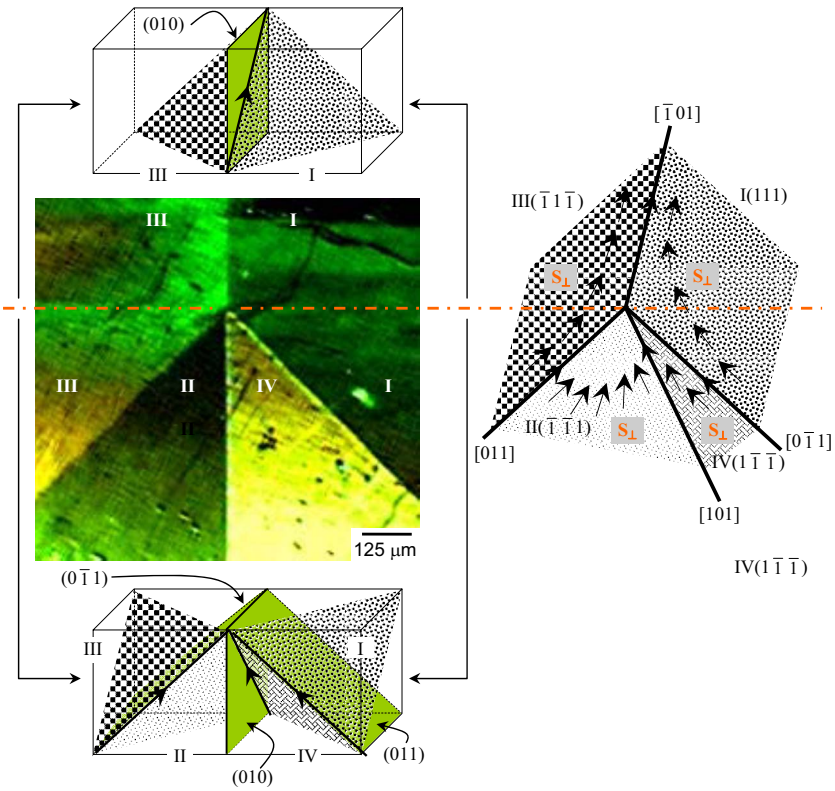

FIG. 5. (Color online) Intersection of four different twin variants at a single point in an annealed NiO single crystal resulting the formation of spin walls. The crystallography of twins below and above the horizontal (orange) line is shown in the respective schematics at the bottom and top. The spin structure around the intersection of the four variants is shown in the schematic on the right; for clarity, the area of twin-II is exaggerated relative to twin-IV.

of the twin domains. Viewed along the [100] direction, the schematic in Fig. 4(b) shows (010) and (110) twin planes. Whereas the projection $P(010)$ of the (010) twin plane on the (100) surface is a straight line, the projection $P(110)$ of the (110) plane on the (100) plane is a band, as shown in Fig. 4(b). From the width of the band, D, the thickness of the crystal can be estimated from the relation $T=D\cos 45°=D/\sqrt{2}$ and is ~ 100 μm. With respect to the notation of twin variants in supplementary document 1,[41] the sequence of variants present in Fig. 4(b) from left to right is III(1$\bar{1}$1)-I(111)-II($\bar{1}\bar{1}$1)-I(111). For the first three variants, III(1$\bar{1}$1)-I(111)-II($\bar{1}\bar{1}$1), in this sequence, Fig. 4(c) shows that the common magnetic axis between twins III and I is [$\bar{1}$01], and the common magnetic axis between twins I and II is [$\bar{1}$10]. Therefore, as shown in Fig. 4(c), the spin direction in the (111) ferromagnetic sheets of twin I must rotate, so that it is able to maintain a common magnetic axis with its neighboring twin III on the left and twin II on the right, thus giving rise to S-domain wall. For the S wall shown in Fig. 4(c), the axis of rotation is perpendicular to the (111) plane. Following the notation by Roth,[6] such S walls are called $S_{\parallel}$ since the wall is parallel to the ferromagnetic sheets; the other variety is called $S_{\perp}$ walls where the wall is perpendicular to the ferromagnetic sheets. Figure 5 shows another annealed sample in which four different twin variants meet at a single point. In this example, the crystallography of the twins below and above the horizontal line is shown in the respective schematics at the bottom and top. The spin structure around the intersection of these four variants is shown in the schematic on the right where, for clarity, the area of twin II is exaggerated relative to twin IV. Figure 5 again highlights the necessity of S walls due to geometrical constraints imposed by T walls.

B. Role of spin and twin walls in observed torque hysteresis in NiO and NiO-Co

Figures 6(a)–6(f) show torque curves of an annealed NiO single crystal, measured at field values ranging from 100 to 50 000 Oe, with applied field confined to the (100) plane of the crystal; although not shown, the torque curve measured at 70 000 Oe had a profile similar to that at 50 000 Oe. These torque curves were measured by rotating the sample both clockwise and counterclockwise about the [100] crystal axis at a given field, with 0° arbitrarily assigned to torque measured along the [010] direction. Note that the shift in torque along the ordinate by $\sim 5.24 \pm 0.56$ nN m is not an accidental consequence of torque chip calibration. Instead, it reflects the asymmetrical twin domain structure present in the sample, as shown in Fig. 7. The torque curves were measured in order of ascending magnetic fields and the domain pattern in the sample was imaged before and after the torque experiments, as shown in Figs. 7(a) and 7(b), respectively. Figure 7(c) is obtained by superimposing Figs. 7(a) and 7(b) in order to show the relative position of twin walls before and after the torque experiments. Optical imaging of T walls as a function of applied field (described later) shows that T walls become mobile when the applied field exceeds $\sim$10 000–20 000 Oe. However, small displacements of T walls may not always be obvious [for instance, the relatively small change in the width of the twin at the right in the superimposed image in Fig. 7(c)] or may be below the resolution of the optical microscope. The field dependence of rotational hysteresis described later in Fig. 10 shows that the threshold for T-wall movement is closer to 10 000 Oe rather than 20 000 Oe; at fields lower than $\sim$10 000 Oe, T walls are essentially frozen and rotational hysteresis arises from S walls.

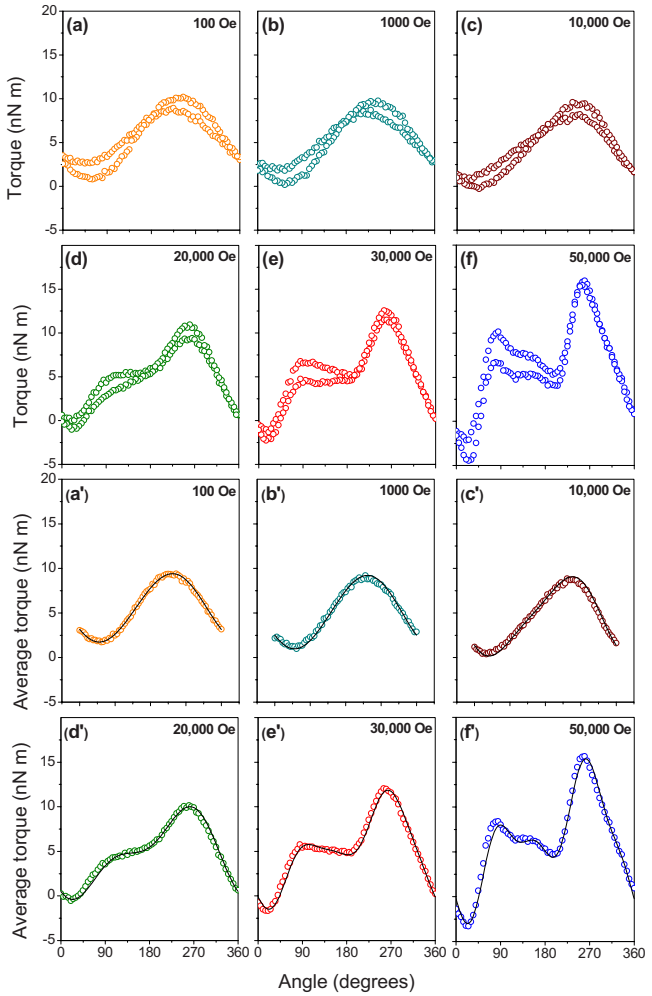

FIG. 6. (Color online) (a)–(f) Torque curves of an annealed NiO single crystal at different field values (shown in each figure). The applied static field was confined within the (100) plane of the crystal, and measurements were made by rotating the crystal about the [100] axis. Corresponding to (a)–(f), (a′)–(f′) show respectively the average torque value at each angle. The solid lines are curve fit to the data (open circles).

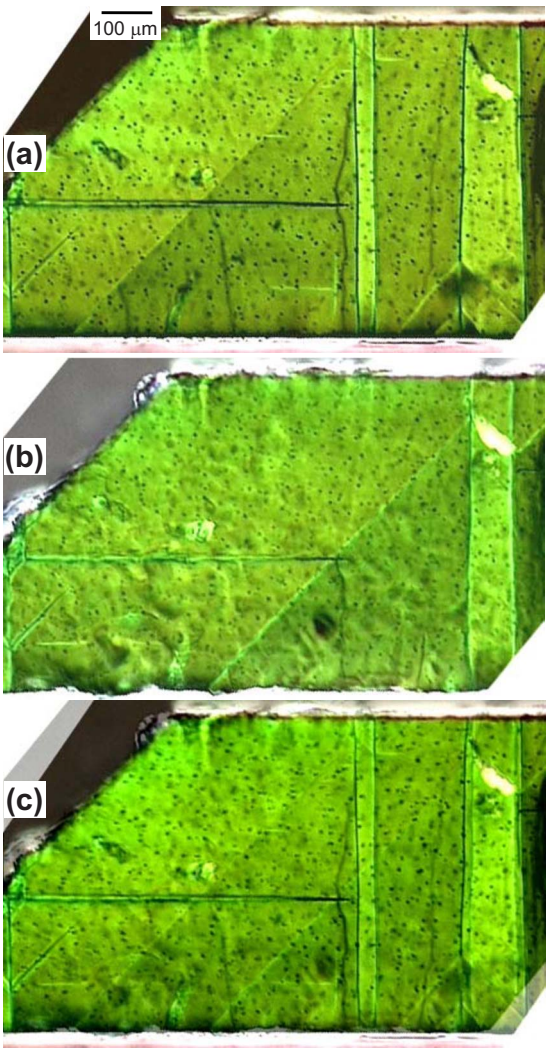

FIG. 7. (Color online) Domain patterns in bare NiO single crystal. (a) Before and (b) after torque measurements shown in Fig. 6. (c) Superimposed image of (a) and (b) showing the relative displacement of T walls as well as nucleation of new twin domains following the torque measurements.

Corresponding to Figs. 6(a)–6(f), Figs. 6(a′)–6(f′) show respectively the so-called "true" torque curves, obtained by taking the average torque value at each angle. The solid lines in Fig. 6(a′)–6(f′) are curve fit to the data (open circles). Figures 6(a′)–6(f′) show that, at fields lower than ~10 000 Oe, the true torque curves are primarily sinusoidal (sin θ) with a small contribution from sin 2θ and has the form $T=|T_o|-|T_1|\sin(\theta+\varphi)-|T_2|\sin 2(\theta+\varphi)$; the phase shift $\varphi(=35°)$ in the fitted curves in Figs. 6(a′)–6(f′) is related to the arbitrarily assigned angle of $\theta=0$ for torque measured along the [010] direction. At higher fields, the sin 2θ and the sin 4θ components become progressively more dominant, and the fitted curves are of the form $T=|T_o|-|T_1|\sin(\theta+\varphi)-|T_2|\sin 2(\theta+\varphi)+|T_3|\sin 4(\theta+\varphi)$.[49] A notable feature of the torque curves in Figs. 6(a)–6(f) is the observation of significant hysteresis even at fields as low as 100 Oe [Fig. 6(a)]. The exciting features of this hysteresis can be seen more clearly from the difference in torque values corresponding to clockwise and counterclockwise rotations, as shown in Figs. 8(a)–8(f). The torque hysteresis curves in Fig. 8 show that at low fields the absolute value of hysteresis versus angle has the form $\sin^2\theta$, which devolves into unidirectional symmetry with the empirical curve fit equation containing components of $\cos\theta$ as well as $\sin^3\theta$. In contrast, the torque curves for NiO-Co (10 nm) system are shown in Figs. 9(a)–9(d). Again, these curves were measured by rotating the sample both clockwise and counterclockwise about the NiO [100] crystal axis, with applied field confined to the (100) plane. Figures 9(a′)–9(d′) shows, respectively, the corresponding torque hysteresis (absolute values) curves obtained from difference in torque values for clockwise and counterclockwise rotations in Figs. 9(a)–9(d); see for comparison torque hysteresis curves for bare NiO single crystal in Fig. 8. The torque curves in Figs. 9(a)–9(d) show that, at fields lower than ~20 000 Oe, the curves are primarily sinusoidal and exhibit higher harmonics at higher fields. Moreover, as expected, the magnitude of the torque in the presence of Co film is more than an order of magnitude higher than that for bare NiO

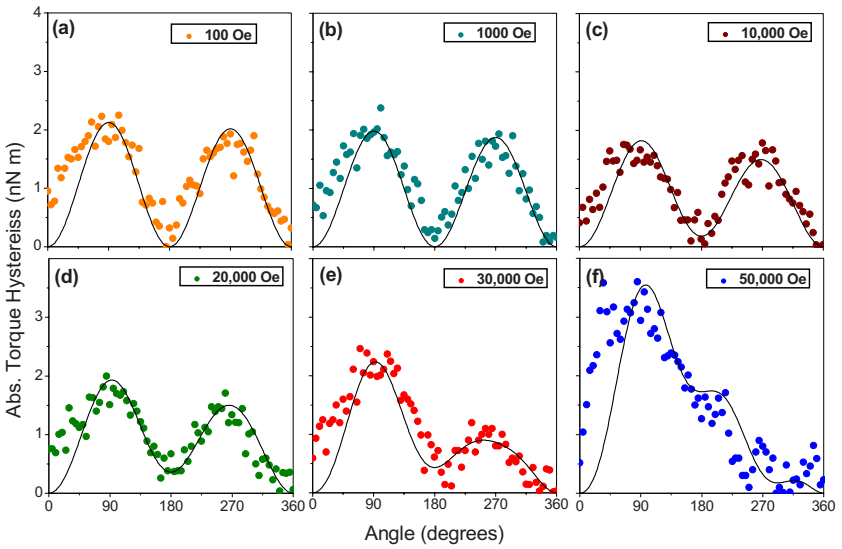

FIG. 8. (Color online) (a)–(f) Torque hysteresis curves of bare NiO crystal obtained from difference in torque values for clockwise and counterclockwise rotation. Curves (a)–(f) correspond to curves (a)–(f) in Fig. 6, respectively. See text for explanation.

crystal in Fig. 6. However, there are two noteworthy features of the torque and the torque hysteresis curves in Fig. 9. First, the angular dependence of torque hysteresis in Figs. 9(a′)–9(d′) is isotropic, in stark contrast to the well-defined symmetrical behavior for the bare NiO crystal in Fig. 8. Second, the magnitude of the torque hysteresis is comparable to that for bare NiO crystal in Fig. 8, being of the order of 0–3 nN m in both cases. In other words, the contribution to torque hysteresis at the measured fields is principally governed by S and T walls in NiO, as further shown in the following.

By integrating the torque hysteresis, $\int Rd\theta$, the total rotational hysteresis W is obtained. Rotational hysteresis is a measure of discontinuous change in magnetization as the sample is rotated in a constant magnetic field. In an ordinary ferromagnet, magnetization rotates continuously at fields higher than its saturation field and rotational hysteresis approaches zero. This is shown in Fig. 10 for a 10-nm-thick Co single film (green, lower curve), where rotational hysteresis is plotted as a function of inverse magnetic field $(1/H)$. The zoomed-in view in the inset of Fig. 10 shows that in-plane rotational hysteresis of Co film tends toward zero at fields in excess of ~1000 Oe $(1/H<0.001\ \text{Oe}^{-1})$ and becomes negligible at fields higher than ~5000 Oe $(1/H<0.0002\ \text{Oe}^{-1})$. *This drop toward zero is the expected behavior of an ordinary ferromagnet*. Figure 10 also plots rotational hysteresis for NiO single crystal and NiO-Co, whose torque characteristics were described in Figs. 6–9. The remarkable feature of Fig. 10 is the "ferromagneticlike" drop in rotational hysteresis for the bare NiO single crystal (blue, upper curve) with increasing field strength (decreasing values of $1/H$), until a threshold field of ~10 000 Oe $(1/H<0.0001\ \text{Oe}^{-1})$ is reached beyond which rotational hysteresis increases abruptly. The stage corresponding to the ferromagneticlike drop in rotational hysteresis is attributed to discontinuous changes in antiferromagnetic spin motif due to motion of S walls, as marked in Fig. 10. In this stage, the density of S walls decreases with increasing field strength (analogous to the process of domain wall annihilation in an ordinary ferromagnet), and rotational hysteresis begins to drops. However, as long as T walls are present, S walls are a geometrical necessity, as discussed in Figs. 4 and 5. Therefore, unlike Co film in Fig. 10, the rotational hysteresis in bare NiO due to S walls does not drop to zero. Instead, S walls migrate from bulk volume of NiO to the T-wall interfaces, and they begin to exert an equivalent mechanical pressure on T walls $(P_W=(\rho H^2/2)[\partial\bar{\chi}(g)/\partial g]$, where the wall pressure P_W is related to the mechanical stress by the relationship $P_W=\sigma_{appl}\frac{\Delta l}{l}$, ρ is the density of NiO and g is the volume fraction of domains of a given orientation in the sample, $\bar{\chi}$ is the average susceptibility of multidomain NiO, and $\frac{\Delta l}{l}(=1.6\times10^{-3})$ is the maximum strain along the $\langle 111\rangle$ direction based on rhombohedral contraction along this axis).[8] At fields on the order of 10 000 Oe, the wall pressure is on the order of ~0.1–0.2 MPa, which is enough to cause T-wall displacement, and consistent with previous studies on stress-mediated motion of T walls.[6,8] Above ~10 000 Oe $(1/H<0.0001\ \text{Oe}^{-1})$, the wall pressure exceeds the threshold value for displacement of T walls in the crystal, resulting in a sharp increase in rotational hysteresis, as marked in Fig. 10. The implication of these results is that as long as T walls are present, S walls are geometrically necessary, and the observed crossover (a drop followed by an abrupt increase) in rotational hysteresis from S walls to T walls will always be present. Figure 10 also shows that rotational hysteresis in NiO-Co mirrors the behavior of bare NiO crystal. Since rotational hysteresis in Co single film is zero at fields higher than 5000 Oe, the observed rotational hysteresis for NiO-Co in Fig. 10 (red, middle curve) is mainly governed by S walls at low fields (<10 000 Oe) and T walls at higher fields.

Figure 10 suggests that if S walls were absent in a bare NiO sample, rotational hysteresis associated with S walls would be zero. This is shown in Fig. 11 for a bare NiO single crystal that was twin free (except for a tiny twin band near one of the four corners of the sample). Figure 11 shows that, indeed, in the absence of geometrical constraints imposed by the T walls, S walls are absent or easily swept away, and the rotational hysteresis associated with S walls is zero or negligible. The inset in Fig. 11 shows a zoomed-in comparative view of rotational hysteresis for this twin-free crystal versus the twinned NiO crystal in Fig. 10. Even though this crystal was twin free, another exciting feature of Fig. 11 is the

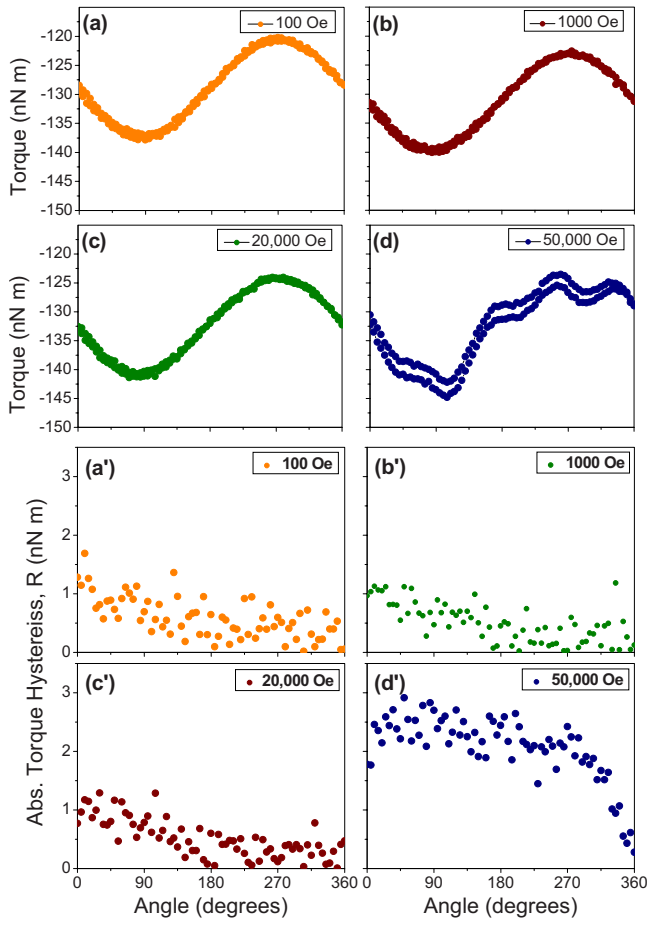

FIG. 9. (Color online) (a)–(d) Torque curves of annealed NiO-Co (10 nm thick) exchange coupled system at different field values (shown in each figure). The applied static field was confined to the (100) plane of the NiO crystal, and measurements were made by rotating the NiO crystal about the [100] axis. (a′)–(d′) show, respectively, the torque hysteresis curves corresponding to (a)–(d). See text for explanation.

abrupt increase in rotational hysteresis from zero to very large values at fields where T-wall motion would prevail. Domain imaging of the crystal following torque measurements revealed the nucleation of several new T walls, which implies the existence of incipient nuclei and embryos of twin domains in the crystal that are too small to be seen by optical microscopy or to impose the necessity of S walls. The inset in Fig. 11 shows that the critical field for heterogeneous nucleation of twin domains from incipient embryos is ~5000–10 000 Oe (0.0002–0.0001 Oe^{-1}). Further studies as a function of applied field and pressure are needed to investigate the nucleation behavior of twin domains and are beyond the scope of the present study.

Note that the low-field torque curves of bare NiO single crystal in Fig. 6 are of the form sin θ (unidirectional). At higher fields, the sin 2θ (uniaxial) component becomes progressively more dominant, which is the expected form of torque curves for an antiferromagnet (H^2 sin 2θ).[7] The low-field sin θ torque curves imply that the following criterion is being met, viz., the applied torque field is less than the threshold field to change the antiferromagnetic spin motif. The present study provides a mechanistic understanding of this "threshold" field in NiO—it is the field required to change the antiferromagnetic spin motif by motion of T walls. Moreover, the sin θ form of torque curves at low fields must also be reconciled with the observed torque hysteresis in Figs. 6 and 8. This can be explained by noting that S walls are geometrically necessary in the presence of T walls. Furthermore, the anisotropy of the (111) plane in NiO is miniscule,[7] which enables S walls to move with ease. As long as the applied field is below the threshold field for T-wall motion, S wall can move back and forth between T walls but it cannot exert enough wall pressure to displace T walls and thereby change the overall antiferromagnetic motif defined by T walls. This explains the hysteretic and largely unidirectional behavior of torque curves at low fields. Only when the applied field for torque measurements exceeds the threshold field for T-wall motion, the torque curves take the expected sin 2θ form (uniaxial), as shown in Fig. 6. This is accompanied by appropriate hysteresis associated with motion of T walls. The unidirectional and the uniaxial behaviors of Co/NiO composite in Fig. 9 parallel the behavior of bare NiO single crystals. The general assumption is that the applied field acts on the ferromagnet, which in turn alters the antiferromagnetic spin structure in exchange anisotropy systems. Instead, *the key point here is that it is vice versa—the applied field acts on the antiferromagnet, which in turn controls the expressions of exchange anisotropy*. Also note that the present study intentionally focuses on {100} surfaces of NiO since they are the fully compensated planes of NiO. This eliminate complications arising from uncompensated spins on NiO surface, such as the {111} surfaces, which can also give rise to a displaced hysteresis loop for NiO/Co and a concomitant unidirectional form of torque curves.

C. Domain walls in exchange coupled Co films originate at twin walls in underlying NiO

Domain walls are also present in Co film exchange coupled to NiO and in the present study they could be annihilated at fields of ~30–100 Oe. In order to understand hysteretic effects associated with domain walls in Co film, their spatial distribution was mapped relative to T walls in NiO, and their field dependence was investigated. For this purpose, 10-nm-thick Co films were sputter deposited on the (100) surface of annealed NiO crystals. The (100) orientation was chosen since it is the fully compensated plane of NiO, as seen from Fig. 1. This eliminates complications arising from uncompensated spins on the NiO surface while at the same time enables the identification of possible pinning sites that may be present on an otherwise compensated surface. Domain walls in Co film were imaged in the reflection mode of the optical microscope. At the same time, the 10-nm-thick Co films were transparent enough to image T domains in the transmission mode of the microscope. This was done simply by switching the light path of the microscope.

Domain studies revealed a one-to-one spatial correlation between domain walls in Co and T walls in underlying NiO, as shown in Figs. 12 and 13. Viewed along the [100] direction, the NiO crystal in Fig. 12(a) consists of a simple plane

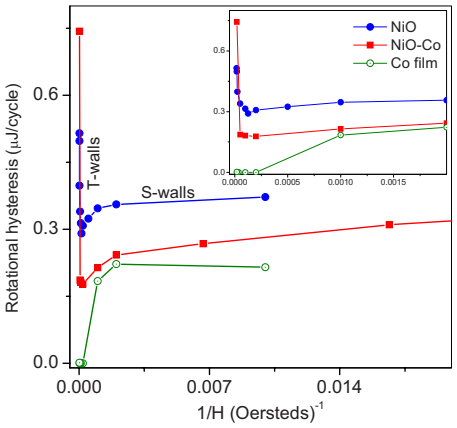

FIG. 10. (Color online) Rotational hysteresis W versus inverse field $(1/H)$ for 10-nm-thick Co single film (green, lower curve), annealed NiO single crystal (blue, upper curve), and annealed NiO-Co (10 nm) exchange coupled system (red, middle curve). The inset shows a zoomed-in view of the curves at high fields. See text for explanation.

parallel assembly of I-III- (or II-IV-) type twin domains across the (010) T walls; the position of T walls is marked by arrows in Fig. 12(a). Figure 12(b) shows the ferromagnetic domain structure in the same area of Co film, which reveals that the domain walls in Co film exactly coincide with T walls in underlying NiO. The domain walls in Co film were imaged in the Nomarski mode of the microscope, which is sensitive to even minute unevenness in surface roughness at the nanometer scale. The surface roughness appears as numerous peaks and valleys in Fig. 12(b) and is to be ignored. It was found that as the underlying T-domain pattern becomes more complex, the domain walls in Co mirrors the same complexity. This is shown in Fig. 13, where twins in NiO are internally twinned, and domain walls in Co assume the same geometrical pattern. Again, ignore the surface roughness features that are enhanced by the Nomarski mode of imaging in the microscope.

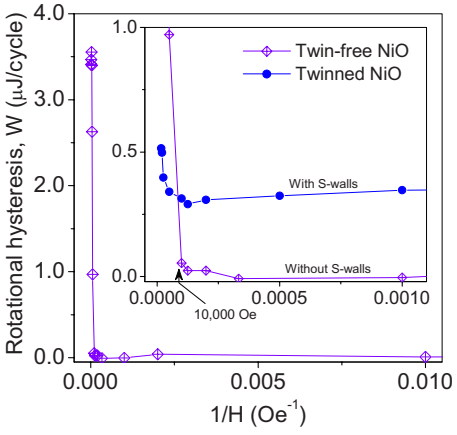

FIG. 11. (Color online) Rotational hysteresis W versus inverse field $(1/H)$ for a twin-free NiO single crystal. In the absence of S walls, rotational hysteresis is zero or negligible until new T domains begin to nucleate at high fields (low $1/H$ values). The inset shows comparative behavior of this twin-free crystal and the twinned NiO single crystals shown in Fig. 10.

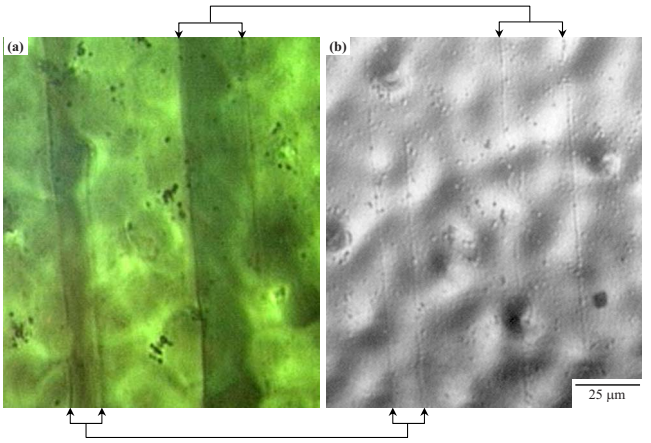

FIG. 12. (Color online) Twin domains and ferromagnetic domains in a NiO-Co (10 nm) exchange coupled system. (a) Plane-parallel assembly of twin domains in NiO as viewed in the transmitted polarized light. The 10 nm Co film on top of NiO is sufficiently transparent in the transmitted mode of the optical microscope and does not interfere with imaging of the T domains. (b) Ferromagnetic domain pattern in Co film imaged in the reflected mode of the microscope. The position of the ferromagnetic domain walls exactly coincides with the underlying T walls.

The field dependence of domain walls in Co film deposited over annealed NiO single crystal is shown in Figs. 14(a)–14(f); the applied field is in the vertical direction. Ignore the diagonal striations in Fig. 14, which are primarily a result of unevenness on the NiO surface over which Co film is deposited. In Fig. 14, the domain walls in Co film run from left to right and map one to one with the underlying twins in NiO (not shown); their position is marked by arrows in Fig. 14(a). Figure 14(b) shows that when the field strength

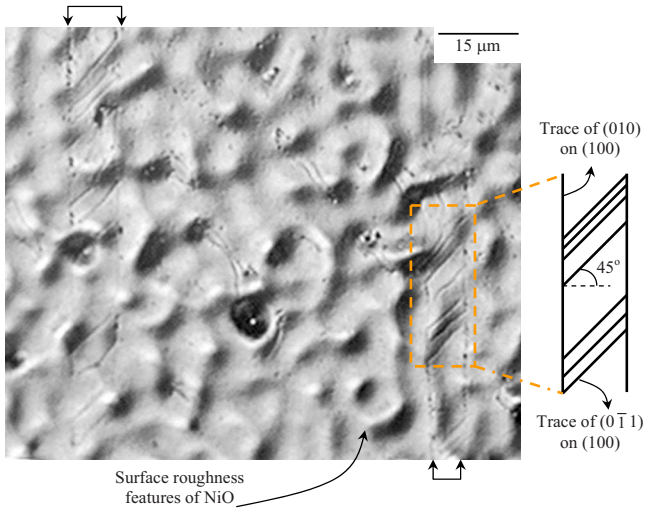

FIG. 13. (Color online) Ferromagnetic domain pattern in Co (10 nm) film deposited on NiO single crystal. The micrograph was recorded in the reflected mode of the optical microscope. Schematic shows that the position of the ferromagnetic domain walls exactly coincides and matches the T-wall geometry in the underlying NiO (not shown). The surface roughness of NiO is enhanced in the Nomarski mode and is to be ignored.

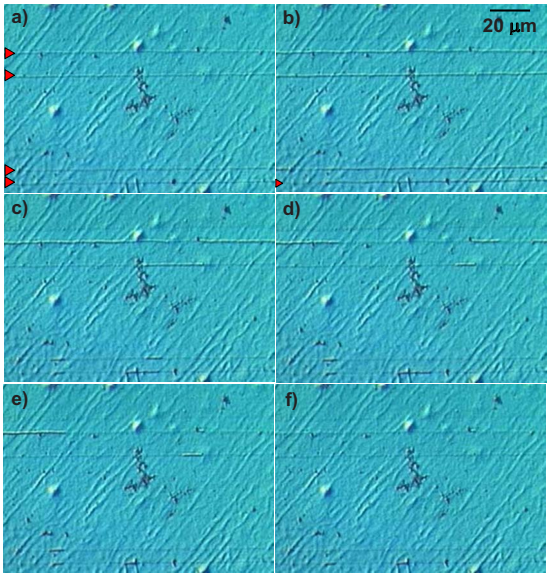

FIG. 14. (Color online) Field dependence of domain walls in Co (10 nm) film deposited on annealed NiO single crystal. The position of the ferromagnetic domain walls exactly coincides with T walls in the underlying NiO (not shown). (a) $H=0$ Oe, (b) $H=-34$ Oe, (c) $H=-38$ Oe, (d) $H=-45$ Oe, (e) $H=-62$ Oe, and (f) $H=-100$ Oe. Applied field is in the vertical direction.

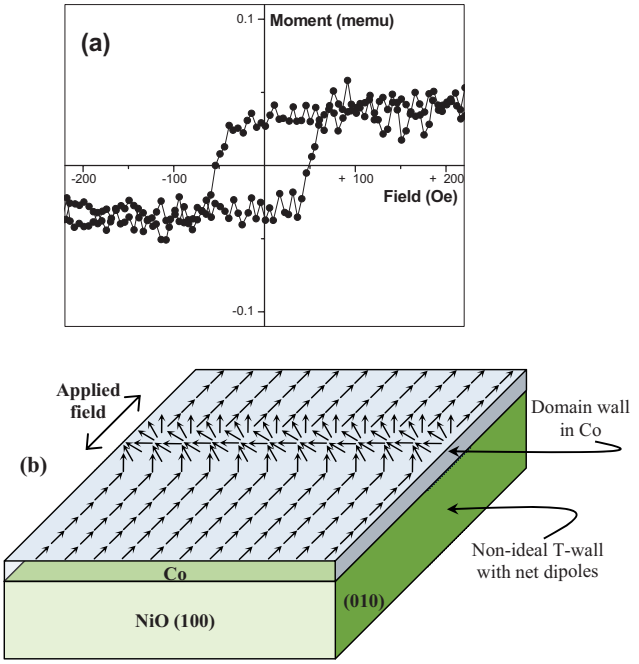

FIG. 15. (Color online) (a) Hysteresis curve of Co (10 nm) thick film sputter deposited on annealed NiO single crystal. (b) Schematic showing domain wall in Co film arising from net dipoles of a non-ideal T wall in underlying NiO.

reaches −34 Oe, a small segment of the domain wall in Co film unpins abruptly, as marked by the red arrow in the lower-left corner of Fig. 14(b). Different segments of domain walls were found to unpin abruptly at different fields until the entire domain walls in Co film disappeared. A movie showing the reversal process is attached along with this paper, which provides details of this abrupt unpinning process more comprehensively. [41] Note that the fields required to unpin the wall segments in Co are much lower than those required to move the underlying T walls in NiO. Moreover, the position of underlying T walls was intermittently monitored by changing the mode of observation from reflected to transmission, and they showed no change in position at these field values. An interesting feature of micrographs in Fig. 14 is the very different behavior of exchange coupled domain walls in Co film compared to walls in a Co single film. In an ordinary ferromagnetic film, domain walls move across the surface of the sample, and domains whose magnetization vector is favorably oriented with respect to the applied field grow and consume domains whose magnetization is unfavorably oriented relative to the field direction. In contrast, domain walls in exchange coupled Co film in Fig. 14 *do not move at all*. Instead, different segments of the domain walls simply unpin at different fields. When the field is turned off, the walls in Co film assumed their original position. As an aid, the measured hysteresis loop of Co-NiO composite is shown in Fig. 15. While the micromagnetic simulations of spins in Co film are beyond the scope of the present study, the schematic in Fig. 15 shows fluctuations in spins in Co film (domain wall) caused by disturbance in an underlying T wall in NiO.

As described in the Introduction, the interface that separates adjacent crystallographic twins also creates a corresponding domain wall (T wall) in the antiferromagnetic spin motif. In the idealized schematics shown in supplementary document 1,[41] the twin interface and the coincident T wall is an atomically sharp plane across which the antiferromagnetic spin motif changes orientation along a common spin axis without a break in continuity. *Only across such an atomically sharp twin interface, T walls would have no net dipoles*. Therefore, at first sight, T walls in NiO are not expected to result in any preferential tendency for pinning of domain walls in Co film and are generally assumed. In contrast, delineation of domain walls in Co film by accumulation of ferrofluid particles in Figs. 12 and 13 clearly reveals that the domain walls in Co film (viewed in reflection mode) coincide with position of underlying T walls in NiO (viewed in transmission mode). This is explained by the fact that twin interface in NiO is not ideal or atomically flat and the atomic positions do not perfectly coincide across the twin wall. Instead, the resulting crystallographic twin walls have a finite width. Since the antiferromagnetic motif is linked to the underlying crystalline motif, the T wall also acquires a finite width and a net dipole. In other words, the finite width of the twin interface can be treated as a long-range defect across which a small net moment exists. Another factor contributing to finite width and net dipoles is the presence of steps in the wall [see, for example, the discussion of varying wall width in Fig. 16 below caused by the presence of (100) steps within the wall]. With a net dipole, the T walls become the preferential sites for formation of domain walls in the Co film. In this picture, the pinning strength would also depend on the orientation of the T walls, {100} versus {110} type, since they have different surface energies and structures (see, for example, Refs. 50–55). Note that in this picture the origin of

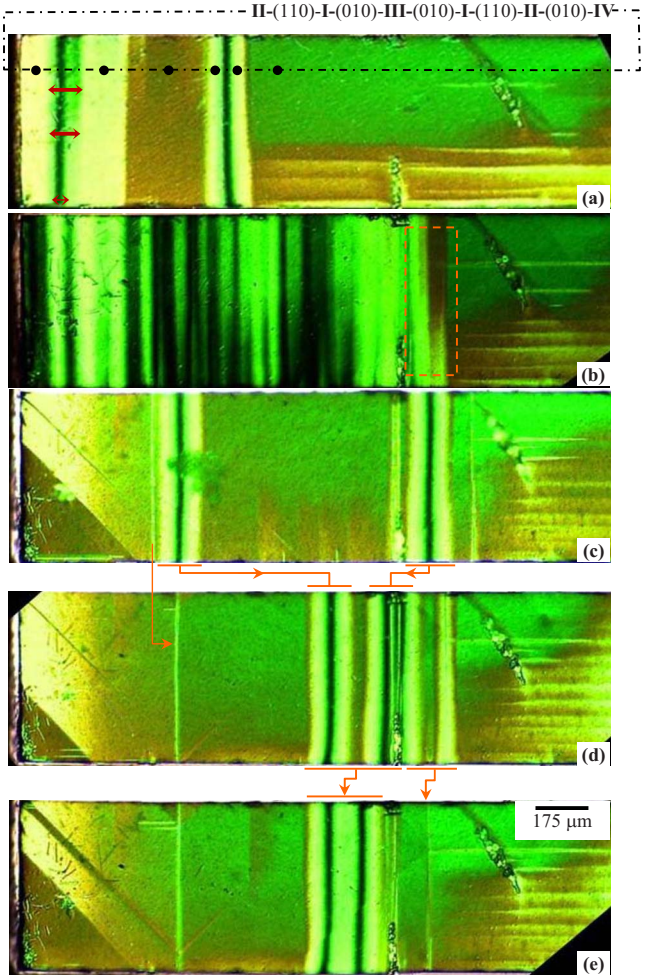

FIG. 16. (Color online) Micromagnetic evolution of T domains in NiO single crystal in magnetic field. [(a),(b)] $H=0$, (c) 3000, (d) 20 000, and (e) 27 000 Oe. See text for explanation of (a) and (b). Applied field is in the vertical direction. See text for explanation.

observed domain wall in Co film in the present study is a magnetic disturbance in the underlying T wall. Once the applied field "smoothens" the effect of this disturbance in the Co film, the wall in Co film ceases to exist. Once the field is removed, the domain wall reappears at the same position. This explains the above described observation that domain walls in Co film do not move at all. At the same time the position of the underlying T wall remains unchanged since the applied fields are less than threshold for movement of T walls.

Previously, the effect of applied field on domain walls has been reported in nanocrystalline or epitaxial systems.[46,56–66] In particular, the observed field dependence of domain walls in Fig. 14 bears key similarities to the author's previously reported results on Co films deposited over *nanocrystalline* NiO films.[46] While the size and the density of ferromagnetic domains are understandably different, in both cases the domain wall motion is not the dominant mode of magnetization reversal (wall motion is entirely absent in the present study while wall motion was occasionally observed in the previous study[46]). Also, in both cases, reversal occurs abruptly and different regions switch at different fields. Moreover, the observed pinning sites are frozen in the applied field range. Despite these "global" similarities, the underlying microstructure of NiO is totally different in these two studies. As opposed to a fixed [100] crystallographic orientation across the NiO-Co interface in the present study, orientation of the nanocrystalline NiO grains changes at the nm scale. A handful of twins exist in the present study that extends the entire length of the crystal that is a few mm long and wide. In contrast, any nanotwin, if present in nanocrystalline NiO, is confined within a grain that is at most a few tens of nm in diameter. Despite these microstructure differences, the observed similarities may be understood by recognizing that a crystallographically ideal T wall has no net dipoles and an ideal T wall would not lead to any preferential tendency for pinning of walls in Co film. Instead, it is the crystallographically imperfect nature of twin interfaces that results in a net dipole and serves as a pinning site for walls in Co film (Figs. 12–14). Other defects can play a similar role, regardless of the scale. Of course, in the case of nanocrystalline NiO, the scale and the density of such pinning sites would be different. The choice of a fully compensated NiO surface in the present study simply helps to eliminate complications and illustrate the commonalities in their observed behavior.

Finally, consider the micromagnetic evolution of T walls in bare NiO single crystals as a function of applied field. It was found that annealed single crystals that were subjected to uncontrolled cooling often resulted in high elastic and magnetic energy domain patterns in which adjacent twins do not share a common magnetic axis of the types shown in supplementary document 1.[41] Such patterns abruptly collapsed into low elastic energy patterns when subjected to relatively low fields. Once the domain pattern collapsed into a low-energy stable configuration, further motion of T walls could only be achieved at fields higher than ~10 000 Oe. This behavior is illustrated in Figs. 16(a)–16(d). Figure 16(a) shows the twin pattern in a NiO single crystal that was cooled from 1673 K at a controlled rate of 5 K/min. The black dots in Fig. 16(a) represents types of twin variants separated by (110)- or (010)-type T walls, as indicated on the top of the figure. For example, the II-I twin on the leftmost portion of Fig. 16(a) is separated by a (110) twin wall. Notice the varying width of this (110) T wall (marked by horizontal arrows), as it gradually tapers toward the bottom. This is caused by the presence of (100) steps in the wall. In contrast, the (110) T wall between the second set of I-II twins in Fig. 16(a) has a more uniform width. The I-(110)-II twin sequence in Fig. 16(a) is a low elastic energy configuration and the I-II twins were found to occur frequently in annealed NiO crystals. The sample shown in Fig. 16(a) was reheated to 1673 K and cooled uncontrollably by opening the furnace door. The resulting twin pattern is shown in Fig. 16(b). The twin pattern in Fig. 16(b) has a high elastic energy as a result of simultaneous nucleation of twins in different volumes of the crystal and their subsequent intersection at crystallographically and magnetically incompatible interfaces. For example, the twins marked in the dotted box in Fig. 16(b) would not ordinarily exist on the basis of continuous transition in antiferromagnetic motifs shown in supplementary document 1.[41] The large variations in color contrast are also indicative of a high internal strain in the crystal. Indeed,

when a small magnetic field of 3000 Oe was applied, the twin assembly in Fig. 16(b) abruptly collapsed into a low-energy twin pattern shown in Fig. 16(c). Following this collapse, no measurable motion of twin walls was detected until the field reached 20 000 Oe. Also notice the presence of two pairs of I-II-type twins in Fig. 16(c), marked by horizontal lines at the bottom. Figures 16(d) and 16(e) show the twin configuration at 20 000 and 27 000 Oe, respectively. The notable feature of the field-induced twin motion is the movement of stable I-(110)-II twin pairs *as a single unit*, as shown sequentially in Figs. 16(d) and 16(e), until they form a plane parallel assembly of I-II-I twins, as seen in the middle of Fig. 16(e). The collapse of unstable twin configuration in Fig. 16(b) at low fields into a stable twin pattern in Fig. 16(c) also helps to explain the initially large hysteresis that is often observed in exchange coupled systems, followed by a decrease in the width of the hysteresis loops with a repeated cycling of the sample.[21–24]

ACKNOWLEDGMENTS

This work was supported by the National Science Foundation Grants No. DMR-0706074 and No. DMR-0305242, and this support is gratefully acknowledged.

*Corresponding author; hchopra@buffalo.edu

[1] R. Gunnarsson and M. Hanson, Phys. Rev. B **73**, 014435 (2006).
[2] Y. I. Latyshev, A. P. Orlov, A. M. Nikitina, P. Monceau, and R. A. Klemm, Phys. Rev. B **70**, 094517 (2004).
[3] F. M. Muntyanu, A. Gilewski, K. Nenkov, A. J. Zaleski, and V. Chistol, Phys. Rev. B **76**, 014532 (2007).
[4] J. D. Livingston and B. Chalmers, Acta Metall. **5**, 322 (1957).
[5] V. Randle, N. Hansen, and D. J. Jensen, Philos. Mag. A **73**, 265 (1996).
[6] W. L. Roth, J. Appl. Phys. **31**, 2000 (1960).
[7] W. L. Roth and G. A. Slack, J. Appl. Phys. **31**, S352 (1960).
[8] G. A. Slack, J. Appl. Phys. **31**, 1571 (1960).
[9] K. Kurosawa, M. Miura, and S. Saito, J. Phys. C **13**, 1521 (1980).
[10] J. Stohr, A. Scholl, T. J. Regan, S. Anders, J. Luning, M. R. Scheinfein, H. A. Padmore, and R. L. White, Phys. Rev. Lett. **83**, 1862 (1999).
[11] H. Matsuyama, C. Haginoya, and K. Koike, Phys. Rev. Lett. **85**, 646 (2000).
[12] F. Nolting, A. Scholl, J. Stöhr, J. W. Seo, J. Fompeyrine, H. Siegwart, J.-P. Locquet, S. Anders, J. Lüning, E. E. Fullerton, M. F. Toney, M. R. Scheinfein, and H. A. Padmore, Nature (London) **405**, 767 (2000).
[13] H. Ohldag, A. Scholl, F. Nolting, S. Anders, F. U. Hillebrecht, and J. Stohr, Phys. Rev. Lett. **86**, 2878 (2001).
[14] C. Tusche, H. L. Meyerheim, F. U. Hillebrecht, and J. Kirschner, Phys. Rev. B **73**, 125401 (2006).
[15] J. Nogues, T. J. Moran, D. Lederman, I. K. Schuller, and K. V. Rao, Phys. Rev. B **59**, 6984 (1999).
[16] W. H. Meiklejohn and C. P. Bean, Phys. Rev. **102**, 1413 (1956).
[17] W. H. Meiklejohn and C. P. Bean, Phys. Rev. **105**, 904 (1957).
[18] W. H. Meiklejohn, J. Appl. Phys. **33**, 1328 (1962).
[19] J. S. Kouvel, Phys. Chem. Solids **16**, 152 (1960).
[20] R. P. Michel, A. Chaiken, C. T. Wang, and L. E. Johnson, Phys. Rev. B **58**, 8566 (1998).
[21] D. Paccard, C. Schlenker, O. Massenet, R. Montmory, and A. Yelon, Phys. Status Solidi **16**, 301 (1966).
[22] C. Schlenker, Phys. Status Solidi **28**, 507 (1968).
[23] C. Schlenker, S. S. P. Parkin, J. C. Scott, and K. Howard, J. Magn. Magn. Mater. **54-57**, 801 (1986).
[24] M. K. Chan, J. S. Parker, P. A. Crowell, and C. Leighton, Phys. Rev. B **77**, 014420 (2008).
[25] R. B. Falk and G. D. Hooper, J. Appl. Phys. **32**, S190 (1961).
[26] I. S. Jacobs and J. S. Kouvel, Phys. Rev. **122**, 412 (1961).
[27] V. S. Speriosu, B. Dieny, P. Humbert, B. A. Gurney, and H. Lefakis, Phys. Rev. B **44**, 5358 (1991).
[28] L. M. Falicov, Phys. Today **45**(10), 46 (1992).
[29] C. G. Shull, W. A. Strauser, and E. O. Wollan, Phys. Rev. **83**, 333 (1951).
[30] P. W. Anderson, Phys. Rev. **79**, 350 (1950).
[31] P. W. Anderson, Phys. Rev. **115**, 2 (1959).
[32] W. L. Roth, Phys. Rev. **111**, 772 (1958).
[33] W. L. Roth, Phys. Rev. **110**, 1333 (1958).
[34] S. Saito, Jpn. J. Appl. Phys. **17**, 1287 (1962).
[35] K. Kurosawa, S. Saito, and S. Takemoto, Jpn. J. Appl. Phys. **13**, 804 (1974).
[36] V. S. Mandel, J. Cryst. Growth **174**, 346 (1997).
[37] M. Foex, C.R. Seances Acad. Sci., Ser. A **227**, 193 (1948).
[38] C. H. La Blanchetais, J. Phys. Radium **12**, 765 (1951).
[39] H. Kondoh, E. Uchida, Y. Nakazumi, and T. Nagamiya, J. Phys. Soc. Jpn. **13**, 579 (1958).
[40] H. P. Rooksby, Acta Crystallogr. **1**, 226 (1948).
[41] See EPAPS Document No. E-PRBMDO-80-067930 for a list of all possible twin configurations corresponding to contraction along the four different ⟨111⟩ axes and for a movie showing the effect of applied field on magnetic domain walls in Co film that are created due to net dipoles in underlying T walls. For more information on EPAPS, see http://www.aip.org/pubservs/epaps.html.
[42] R. Newman and R. M. Chrenko, Phys. Rev. **115**, 882 (1959).
[43] R. Newman and R. M. Chrenko, Phys. Rev. **114**, 1507 (1959).
[44] U. Hartmann and H. H. Mende, J. Phys. D **18**, 2285 (1985).
[45] H. D. Chopra, M. R. Sullivan, A. Ludwig, and E. Quandt, Phys. Rev. B **72**, 054415 (2005).
[46] H. D. Chopra, D. X. Yang, P. J. Chen, H. J. Brown, L. J. Swartzendruber, and W. F. Egelhoff, Jr., Phys. Rev. B **61**, 15312 (2000).
[47] M. R. Sullivan and H. D. Chopra, Phys. Rev. B **70**, 094427 (2004).
[48] F. Bitter, Phys. Rev. **38**, 1903 (1931).
[49] Whereas the coefficient for the $\sin\theta$ term (T_1) is $\sim 4.09 \pm 0.21$ nN m at all fields, the coefficient for the $\sin 2\theta$ term (T_2) increases from ~ 0.1 nN m (or 2.5% of T_1) at low fields to 4.7 nN m ($\sim 115\%$ of T_1) at 50 000 Oe. The coefficient T_3 for the $\sin 4\theta$ term is ~ 0.15 and 1.5 nN m at 30 000 and 50 000 Oe, respectively, and is approximately zero at lower fields.

[50] D. Wolf, Mater. Sci. Res. **14**, 13 (1981).
[51] D. Wolf, Adv. Ceram. **10**, 290 (1984).
[52] D. Wolf, Solid State Ionics **75**, 3 (1995).
[53] D. J. Coates, J. W. Evans, and K. H. Westmacott, J. Mater. Sci. **17**, 3281 (1982).
[54] G. Dhalenne, A. Revcolevschi, and A. Gervais, Phys. Status Solidi A **56**, 267 (1979).
[55] H. Schmid, M. Ruehle, and N. L. Peterson, Mater. Sci. Res. **14**, 177 (1981).
[56] N. Rougemaille, M. Portalupi, A. Brambilla, P. Biagioni, A. Lanzara, M. Finazzi, A. K. Schmid, and L. Duo, Phys. Rev. B **76**, 214425 (2007).
[57] S. W. Kim, S. S. Lee, R. D. Gomez, E. J. Hahn, and D. G. Hwang, Phys. Status Solidi A **203**, 2078 (2006).
[58] U. Welp, S. G. E. te Velthuis, G. P. Felcher, T. Gredig, and E. D. Dahlberg, J. Appl. Phys. **93**, 7726 (2003).
[59] J. P. King, J. N. Chapman, M. F. Gillies, and J. C. S. Kools, J. Phys. D **34**, 528 (2001).
[60] F. Bisio, L. Anghinolfi, M. Canepa, and L. Mattera, Phys. Rev. B **79**, 054407 (2009).
[61] J. Camarero, J. Miguel, J. B. Goedkoop, J. Vogel, F. Romanens, S. Pizzini, F. Garcia, J. Sort, B. Dieny, and N. B. Brookes, Appl. Phys. Lett. **89**, 232507 (2006).
[62] F. Romanens, S. Pizzini, F. Yokaichiya, M. Bonfim, Y. Pennec, J. Camarero, J. Vogel, J. Sort, F. Garcia, B. Rodmacq, and B. Dieny, Phys. Rev. B **72**, 134410 (2005).
[63] J. Sort, A. Hoffmann, S.-H. Chung, K. S. Buchanan, M. Grimsditch, M. D. Baró, B. Dieny, and J. Nogués, Phys. Rev. Lett. **95**, 067201 (2005).
[64] O. Hellwig, S. Maat, J. B. Kortright, and E. E. Fullerton, Phys. Rev. B **65**, 144418 (2002).
[65] L. Wee, R. L. Stamps, and R. E. Camley, J. Appl. Phys. **89**, 6913 (2001).
[66] V. I. Nikitenko, V. S. Gornakov, L. M. Dedukh, Y. P. Kabanov, A. F. Khapikov, A. J. Shapiro, R. D. Shull, A. Chaiken, and R. P. Michel, Phys. Rev. B **57**, R8111 (1998).